


ORIGINAL ARTICLE

Open Access



A conjugated structure discloses interaction between two fault systems in eastern Taiwan during 2022 Guangfu earthquake

Chih-Heng Lu¹, Yi-Chun Hsu², Chung-Pai Chang^{2*}  and Yue-Gau Chen¹

Abstract

The Longitudinal Valley (LV) in the eastern Taiwan is located at the convergent boundary between the Philippine Sea Plate and the Eurasian Plate. Within the LV, two significant fault systems, the Longitudinal Valley Fault (LVF) in the eastern part and the Central Range Fault (CeRF) in the western part, have been recognized. However, understanding the precise mechanisms and spatial relationships of the two fault systems in the middle segment of the LV has remained a challenge. In this study, we integrate various data sources, including geodetic measurements, seismic data, field investigations, and simulation results, all obtained during the 2022 Guangfu earthquake event. Our goal is to shed light on the complex structural interactions between the two fault systems. We introduce a coupled structural model consisting of a main fault plane and a coupled ramp plane. The deep-seated fault plane is constrained using seismic data, while the shallow ramp plane is determined through field investigations. Geodetic measurements are utilized to constrain the surface deformation resulting from dislocation model. The simulation outcomes reveal that the 2022 Guangfu earthquake was primarily triggered by the activity along the CeRF. The CeRF experienced an eastward reverse slip of approximately 58 cm along the fault plane. This fault not only intersects the LVF beneath the Coastal Range but also initiates the development of a ramp plane along pre-existing fault planes of the LVF. This intricate interplay results in approximately 20 cm of vertical surface deformation within the Coastal Range. The linear connection observed in the simulation residuals is associated with pre-existing faults within the LVF system. This alignment corresponds to the ground distribution of ramp plane, suggesting that older fault systems within this area exhibit characteristics of reactivation in response to earthquake-induced processes. Our study not only pinpoints the potential location of the CeRF intersecting with the LVF in the middle segment of the LV but also provides insight into one of the interaction mechanisms between the CeRF and the LVF. These findings hold significant implications for assessing seismogenic structural activity and enhancing the mitigation of regional earthquake hazards in the future.

Keywords InSAR, GNSS, Dislocation model, Conjugated structure, 2022 Guangfu earthquake

1 Introduction

On June 20, 2022, the M_L 6.0 Guangfu earthquake, located in the Longitudinal Valley (LV), struck eastern Taiwan with focal depth of 6.8 km. The maximum seismic intensity reached a level of 5 weak in the Hualien region. Notably, this earthquake represents the first occurrence of a seismic event exceeding a magnitude of 6 in the middle segment of the LV since 2013 Ruisui earthquake (Chuang et al. 2014; Lee et al. 2014). Prior researches

*Correspondence:

Chung-Pai Chang
cpchang@csrsr.nctu.edu.tw

¹ Research Center for Environmental Changes, Academia Sinica, Taipei, Taiwan

² Center for Space and Remote Sensing Research, National Central University, Taoyuan, Taiwan



have identified two fault systems beneath the LV: the Longitudinal Valley Fault (LVF) and the Central Range Fault (CeRF) (Kuochen et al. 2004; Shyu et al. 2005; Huang and Wang 2022). The LVF is situated beneath the Coastal Range (CoR) on the eastern side of the LV, characterized as a left-lateral thrust fault with an eastward dip, extending approximately 150 km (Chen et al. 2007, 2018). Meanwhile, the CeRF is located beneath the Central Range (CeR) on the western side of the LV, spanning 85 km. The CeRF is also a thrust fault, but it dips westward and runs in parallel with the LVF (Shyu et al. 2006a, 2016).

Based on the focal mechanism provided by the Broadband Array in Taiwan for Seismology (BATS) and the subsequent distribution of aftershock epicenters (Fig. 1), the seismic event is associated with the reverse faulting activity of the CeRF. This fault has a strike direction of N60°E and a westward dip of approximately 30°, resembling the tectonic structure observed during the 2013 Ruisui Earthquake (Chuang et al. 2014; Lee et al. 2014). Following the earthquake, the Geological Survey and Mining Management Agency (GSMMA) promptly conducted field surveys. The primary surface ruptures were

observed along the Lingding Fault in the northern epicenter and distributed within the Hualien River bed (GSMMA 2022a). The areas surrounding these surface rupture locations exhibited the soil liquefaction phenomena. It is evident that ground shaking was the main cause of these surface ruptures. Consequently, the GSMMA suggests that the earthquake is highly likely to be associated with the activity of the CeRF, which may have triggered the activity of the Lingding Fault (GSMMA 2022a).

However, the geodetic measurements, such as GNSS and leveling, for coseismic surface deformation (GSMMA 2022b) record significant surface deformation not only along the Lingding Fault and Ruisui Fault but also within the CoR. This indicates that the earthquake may have potentially triggered other structures within the CoR in addition to the Lingding Fault. In the middle segment of the LV, the tectonic structures are primarily inferred through geophysical data, including geodetic measurement, seismic relocation, and seismic tomography. Actual geological data are often used only for validation purposes, and as a result, the tectonic structure descriptions may oversimplify the complex interaction between the CeRF and LVF. These limitations pose

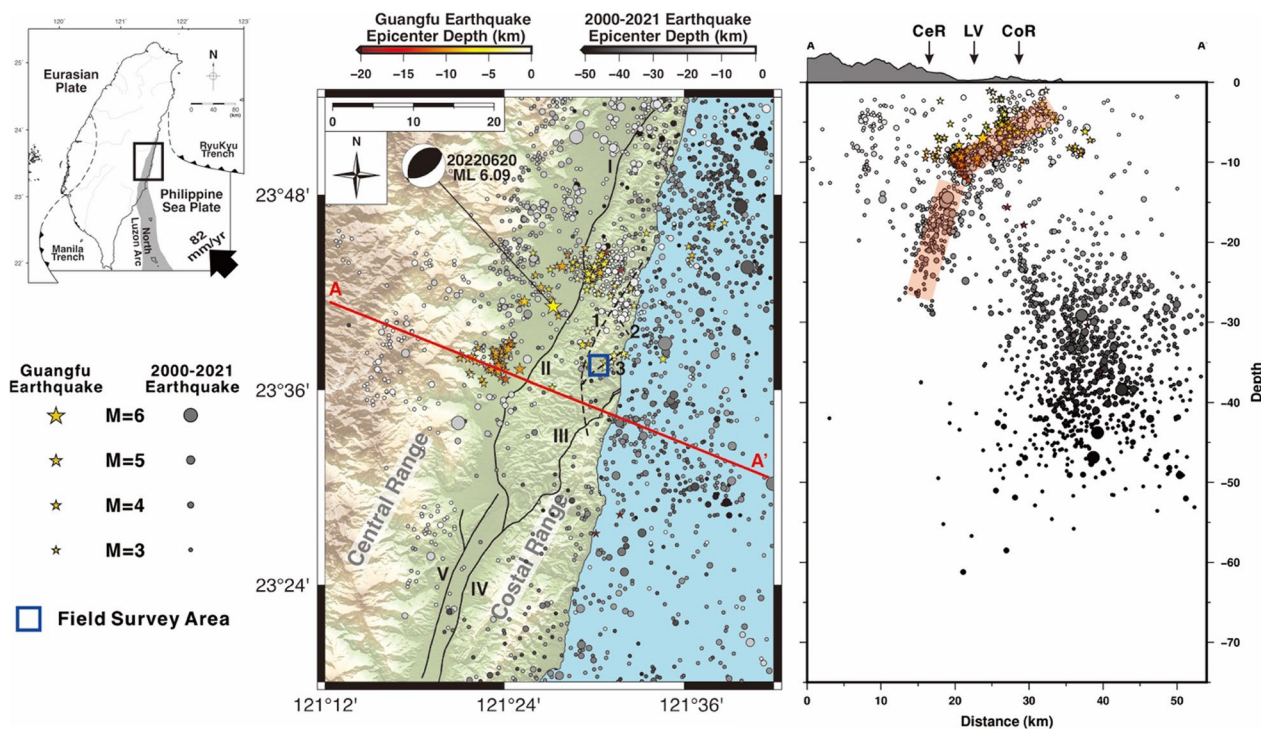


Fig. 1 The study area and seismic data. The warm-colored stars present the earthquake events greater than $M_L = 3$ occurred during the Guangfu earthquake period from BATS. The gray circles present the background seismic events greater than $M_L = 3$ between 2000 and 2021 from Taiwan Geophysical Database Management System, Central Weather Administration. The blue square designates the field survey area. The Roman numerals indicate the active faults (Lin et al. 2021): I. Lingding Fault, II. Ruisui Fault, III. Chimei Fault, IV. Chihshang Faults, and V. Yuli Fault. The Arabic numerals presents the other faults (Hsu 1956): 1. Chichi Fault, 2. Hsinshu Fault, and 3. Kunghsia Fault. The AA' profile represents the projected results of seismic data in the study area. The light red rectangles in the AA' profiles represent the both shallow and deep seismic structures

challenges in comprehensively understanding the conjugated interactions between both fault systems and their associated behaviors.

To address these limitations, this study integrates seismic data, geodetic measurements, and field investigations from the 2022 Guangfu earthquake to constrain the geometric characteristics of subsurface fault planes. By inversion of fault slip and the simulating surface deformation, this research aims to provide insights into the conjugate mechanisms and locations of both fault systems in the middle segment of the LV. These critical details are essential for advancing our understanding of active tectonic processes in the region and their potential implications for seismic hazards.

2 Tectonic background

The LV in eastern Taiwan is situated at the convergent boundary between the Eurasian Plate and the Philippine Sea Plate. The Philippine Sea Plate is heading northwestward at an approximate rate of 8 cm/year (Yu et al. 1997; Yu et al. 2001). This tectonic collision has resulted in the CoR thrusting over the CeR with an angle of 290° (Chen et al. 2007). Over the past seven decades, this region has experienced several large earthquakes with magnitudes greater than 6, including the 1951 Hualien-Taitung earthquakes (Hsu 1962; Shyu et al. 2007; Chung et al. 2008), the 2003 Mw 6.8 Chengkung earthquake (Kuo-Chen et al. 2007), the 2006 Mw 6.1 Taitung earthquake (Wu et al. 2006), the 2013 Mw 6.2 Ruisui earthquake (Chuang, et al. 2014; Lee et al. 2014), and the 2018 Mw 6.4 Hualien earthquake (Yen et al. 2019; Kuo-Chen et al. 2019). These events underscore the ongoing and highly active tectonic processes in the region. Consequently, the LV has long been a subject of scientific interest as a seismogenic structure zone (Cheng and Wang 2001; Kuo-Chen et al. 2004; Shyu et al. 2006a; Rau et al. 2007).

Beneath the LV, two fault systems are present: the LVF and the CeRF. The LVF, which includes Lingding Fault, Ruisui Fault, Chimei Fault, and Chihshang Fault, is primarily located beneath the CoR on the eastern side of the LV. The fault is characterized as a left-lateral thrust fault with an eastward dip angle ranging from 45 to 75°, becoming steeper as it extends from south to north (Chen et al. 2007, 2018). Historical earthquakes such as the 1951 Hualien-Taitung earthquakes and the 2003 Chengkung earthquake provide clear evidence of the continued activity along the LVF. On the other hand, the CeRF including Yuli Fault is located at the western edge of the LV and exists beneath the CeR. The CeRF is a thrust fault with a westward dip angle of 45°, extending to a depth of 20 km (Shyu et al. 2006a, 2016). Several significant earthquakes, including the 2006 Taitung earthquake, the 2013 Ruisui earthquake, and the 2018 Hualien earthquake, have been

attributed to the activity of this fault system. The probabilistic seismic hazard assessment for 2020 published by Taiwan Earthquake Model (TEM PSHA2020) indicates that both the LVF and the CeRF exhibit a high potential for seismic hazard (Chan et al. 2020). Therefore, the interactions between both fault systems not only directly impact the seismogenic activity throughout the entire LV but also contribute to regional seismic hazards.

Previous research has revealed that in the northern segment of the LV, the CeRF is thrusting over the LVF, while in the southern segment, the LVF thrusts over the CeRF (Kuo-Chen et al. 2004; Wu et al. 2006; Kuo-Chen et al. 2019; Shyu et al. 2016, 2020). Huang and Wang (2022), utilizing seismic data from 2018 to 2021 in the middle to northern segments of the LV, propose that the two fault systems intersect approximately in the middle segment of the LV, and suggest a model in which the CeRF cuts across the LVF. Additionally, the Taiwan active faults map (Lin et al. 2021) indicates that both fault systems coming to the surface on either side of the middle segment of the LV, with a narrow width of approximately 3 km. These research findings collectively emphasize that the middle segment of the LV is a critical zone where the two fault systems interact.

Chuang et al. (2014) and Lee et al. (2014), utilizing analyses of focal mechanisms, strong-motion data, surface deformation data, and other relevant factors, concluded that the 2013 Ruisui earthquake in the middle segment of the LV was induced by the CeRF. It is important to note that the tip of CeRF extended beneath the CoR without coming out from the LV. The historical earthquake catalogue between 2000 and 2021 from Taiwan Geophysical Database Management System, Central Weather Administration in this area (Fig. 1) illustrate that the shallow seismic structures with low-angle westward tilting (at depths ranging from 3 to 10 km) and the deep seismic structures with steep-angle westward tilting (at depths exceeding 10 km). However, determining the dip angles of fault planes at depths within 3 km beneath surface challenges due to the limitation in the resolution of seismic data. Consequently, when employing a single fault plane model to simulate surface displacement values, discrepancies may arise not only between the simulation results and actual surface deformations but also in fully considering the true subsurface geological characteristics.

From a structural geological perspective, the Chimei Fault is indeed a distinctive feature in the middle segment of the LV. It stands as the sole branching fault within the entire LVF, and transect the CoR. The Chimei Fault is classified as a type II active fault, with a strike ranging from N10°E to N20°E, a dip angle of 70°S, and a left-lateral slip behavior (Lin et al. 2009, 2021). Shyu et al.

(2006b) conducted an analysis of the river terrace topography in the Hsiukuluan canyon and proposed a fault-bend fold model. This model aids in reconstructing the near-surface geometry of LVF beneath the CoR, specifically in the western portion of the Chimei Fault. Hence, it became evident that the near-surface structural activity beneath the CoR in the middle segment of the LV should be influenced not only by the CeRF, but also impacted by the presence of the LVF.

Furthermore, to the north of the Chimei Fault within the CoR, several small linear structures, such as the Chichi Fault, Hsinshe Fault, and Kunghsia Fault, have also been proposed by the previous study (Fig. 1; Hsu 1956). The Chichi Fault is a NNE striking thrust fault, while the Hsinshe Fault and Kunghsia Fault are both normal faults, with northwest trending and northeast trending, respectively. Later researchers (Wang and Chen 1993; Yi et al. 2012) combined the Chichi Fault and Hsinshe Fault into a single thrust fault and removed the Kunghsia Fault. This indicates that the fault structures in this region are unclear and not fully understood.

3 Geodetic measurements

3.1 DInSAR processing

The radar satellite geodesy for surface deformation has dramatically improved over past three decades, with the SAR interferogram becoming an indispensable tool for monitoring the active tectonic processes (Elliott et al 2016; Biggs and Wright 2020). To capture the coseismic and postseismic surface deformation, we acquired two TOPS (Terrain Observation by Progressive Scans) mode images of Sentinel-1A satellite (operated by the European Space Agency) on June 12th and June 30th, 2022 in the ascending orbit, and two ScanSAR mode images of ALOS-2 satellite (operated by Japan Aerospace Exploration Agency) on April 3rd and September 18th, 2022 in the descending orbit. The wavelengths of Sentinel-1A and ALOS-2 are 5.6 cm and 23.5 cm, respectively. Sentinel-1A offers a spatial resolution of 5×20 m (range \times azimuth), while ALOS-2 provides a resolution of 19×29 m (range \times azimuth). More detailed information for both radar images were listed in Table 1.

The interferometric phases of both satellite images were processed using GMTSAR software version 6.1 (Sandwell et al 2011). We utilized the digital elevation

model (DEM) with a 20 m resolution from the Department of Land Administration, Ministry of the Interior, Taiwan, to remove the topographic phase and correct the geometric effects. The precise orbits were applied for image coregistration and orbit ramp removal. For the phase unwrapping, we employed Snaphu 1.4.2 (Chen and Zebker 2002) and set the coherence threshold to 0.1. While choosing a lower coherence value would result in selecting more noisy pixels and potentially reduce the accuracy of line-of-sight (LOS) displacement calculations, it was necessary to use a more lenient threshold to ensure successful phase unwrapping and capture a higher volume of phase information in the CoR, reducing the likelihood of phase unwrapping failures.

Additionally, we employed ALOS-2 satellite images in a different flight direction to validate the phase results obtained from Sentinel-1A in the CoR. The L-band has superior penetration capabilities through vegetation compared to C-band, allowing for better reception of reflected signals. In the northern LV, ALOS-2 image pairs were successful to map the coseismic surface deformation caused by the 2018 Hualien earthquake (Yen et al. 2019), even with the time intervals exceeding one year. The temporal decorrelation had minimal impact on the coherence, making it a suitable resource for measuring surface deformation induced by co- and post-seismic effects during the current earthquake event.

3.2 GNSS data

The coseismic records of continuous GNSS were collected by the GSMMA, Central Weather Administration, Institute of Earth Sciences of Sinica Academia, and Industrial Technology Research Institute (GSMMA 2022b). These data were subsequently processed using the GipsyX software (Bertiger et al. 2020). The coseismic displacement derived from the continuous GNSS is determined by calculating the difference between the 7-day average before the earthquake (2022/06/13–2022/06/19) and 5-day average after the earthquake (2022/06/20–2022/06/25). Four continuous GNSS stations (FLNM, DNFU, FONB, and JPEI) were selected within the study area to validate the LOS results from Sentinel-1A and the surface deformation simulations.

During the coseismic period, the maximum horizontal displacement was observed to be 32 mm in the southeast

Table 1 The information of Sentinel-1A and ALOS-2

Satellite	Master image date	Secondary image date	Wavelength (cm)	Perp. baseline (m)	Looking angle (°)	Azimuth direction (°)	Diff. days
Sentinel-1A	20220618	20220630	5.6	− 3.7	42	− 12	12
ALOS-2	20220403	20220918	23	128.3	37	− 168	144

direction at FLNM station, while the maximum vertical displacement recorded an uplift of 138 mm at DNFU station. To ensure consistency between the 3D displacements obtained from GNSS data and the 1D displacement in the LOS direction captured by Sentinel-1A, the transition was made to account for the geometric relationship between the satellite’s attitude and the land surface. This transition of 3D displacements was crucial for validating the LOS results. For detailed information on GNSS stations in the coseismic period, please refer to Table 2.

Additionally, the same four continuous GNSS stations were utilized during the co- and post-seismic period to validate the LOS results obtained from ALOS-2. The co- and post-seismic data from GNSS stations were sourced from the Taiwan Geodetic Model, Institute of Earth Science, Academia Sinica, Taiwan (<https://tgm.earth.sinica.edu.tw>) between June 2022 and September 2022. The 3D displacement obtained from continuous GNSS is determined by calculating the difference between the beginning of June (2022/06/01–2022/06/05) and the middle of September (2022/09/13–2022/09/17). The co- and post-seismic displacements recorded by the four GNSS stations are listed in Table 3.

3.3 Comparison DInSAR and GNSS

In Fig. 2a–d, we present the interferograms and LOS results obtained from Sentinel-1A and ALOS-2. Both DInSAR results reveal significant surface deformation

not only along the Lingding Fault and Ruisui Fault but also within the CoR, with the largest surface displacement occurred approximately 5 km southeast of the epicenter. Generally, the fringe numbers in Sentinel-1A data are four times larger than those in ALOS-2 data. This disparity can be attributed to the fact that the wavelength of ALOS-2 is four times longer than that of Sentinel-1A. While the differences in phase patterns between the two kinds of satellite images may arise from factors such as opposite flight directions, varying look angles, and surface deformation over time, it’s important to note that both DInSAR results exhibit discontinuous fringe line in the CoR with NNE direction that coincide with the Hsin-she Fault and Kunghsia Fault (Fig. 2a and b). This finding suggests that these old faults act as barriers, limiting the propagation of surface deformation towards the eastern side of the CoR.

The primary deformation zone observed in the Sentinel-1A LOS results extends across the RSF and is distributed in the LV plain and CoR (Fig. 2c). Conversely, the primary displacements in the ALOS-2 LOS results are concentrated in the CoR (Fig. 2d). Both LOS results indicate significant shortening displacements in the same region within the CoR, with values approaching 200 mm. To validate the LOS results, the 3D displacements obtained from GNSS data were projected into LOS direction for both satellite orbits, using the FLNM station as the reference point. The comparison between GNSS LOS results and both satellite LOS results demonstrates

Table 2 The information of GNSS stations during coseismic period

GNSS station	Longitude	Latitude	3D displacements (mm)			Projected to LOS (mm) Ascending orbit for Sentinel-1A
			E-W	N-S	U-D	
DNFU	121.48229	23.68513	37.23	− 5.32	134.59	92.66
FLNM	121.45336	23.74631	10.04	− 22.09	− 0.75	− 15.09
FONB	121.52095	23.59816	− 0.88	4.98	4.89	6.77
JPEI	121.37140	23.53160	− 3.59	− 8.15	− 3.41	0.74

Table 3 The information of GNSS stations during co- and post-seismic periods

GNSS station	Longitude	Latitude	3D displacements (mm)			Projected to LOS (mm) Descending orbit for ALOS-2
			E-W	N-S	U-D	
DNFU	121.48229	23.68513	58.43	− 23.04	85.53	105.60
FLNM	121.45336	23.74631	21.54	− 34.11	− 8.15	10.44
FONB	121.52095	23.59816	− 36.65	46.49	− 5.51	− 31.80
JPEI	121.37140	23.53160	− 8.51	− 15.08	7.67	3.01

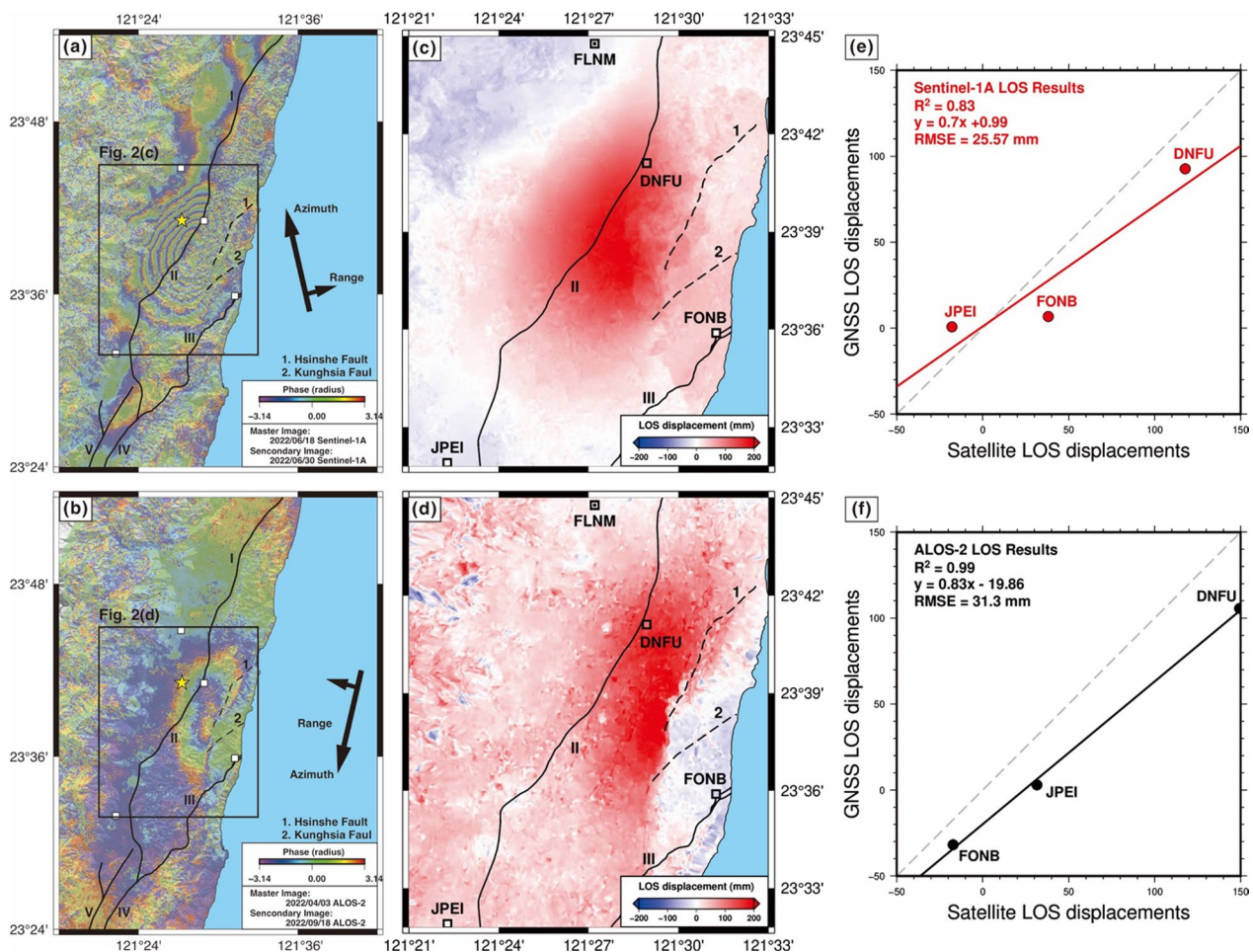


Fig. 2 Geodetic measurement results. **a** Sentinel-1A ascending and **b** ALOS-2 descending interferometric results. The dashed-lines indicate the Hsinhshe Fault and Kunghsia Fault. **c** Sentinel-1A ascending and **d** ALOS-2 descending LOS results. The warm and cold colors indicate the decrease and increase displacements in the LOS direction, respectively. The squares are the GNSS stations and the 3D displacements obtained from GNSS were projected to LOS direction, especially GNSS station—FLNM is setting as the reference point. The comparison between GNSS LOS data and both satellite LOS results: **e** Sentinel-1A and **f** ALOS-2

a good fit, with slope values ranging from 0.7 to 0.83, R^2 values ranging from 0.83 to 0.99, and root mean square error of less than 32 mm (Fig. 2e and f).

Additionally, both LOS results reveal a noticeable linear boundary along HSF and KHF between DNFU and FONB. On the eastern side of this linear boundary, LOS results generated by coseismic effects for the ascending orbit indicated movement toward the satellite, with displacements of approximately 50 mm. Conversely, LOS results influenced by co- and post-seismic effects for the descending orbit show movement away the satellite, with displacements of around 60 mm. The records from the FONB station shown in Tables 2 and 3 indicate that the surface activity characteristics in this region vary between two different observation periods. The variation in surface deformation over time highlights the

distinctive characteristics of co- and post-seismic stages along this linear boundary.

4 Field observation

Based on the fault geometry observed during the 2013 Reisu earthquake event (Chuang et al. 2014; Lee et al. 2014), if the low-angle westward dipping fault were to extend to the surface, the surface rupture should theoretically occur in the Pacific Ocean to the east of the CoR. However, the observed discontinuous interferometric fringe patterns from both DInSAR results were located within the CoR. Therefore, we propose a hypothesis suggesting the presence of a high-angle fault connecting to the low-angle fault. This high-angle fault would extend westward and simultaneously surface to the east in the near-surface shallow area.

The outcrop of this high-angle fault may relate to the northern segment of the Chimei Fault, which is close to the Kunghsia Fault (Hsu 1954, 1956). The strike of the Kunghsia Fault is NE direction, and the northwest side is the uplift side (Hsu 1956; Fig. 3a). Wang and Chen (1993) did not propose this fault in their study, possibly because this fault is not easily observable in the field. As a result, the Kunghsia Fault has remained a questionable structure. However, the eastern linear boundary of the coseismic surface deformation in this earthquake is closely adjacent to the fault lines (Fig. 2c and d), indicating that Kunghsia Fault has the potential for reactivation.

Detailed field investigations are required to understand the geometry and mechanics of the Kunghsia Fault.

Our investigation area is in the Valley of Tingtzelou river (Fig. 3a), is composed of Plio-Pleistocene Paliwan Formation, and mainly lithological composition is sandstone interbedded with shale (1/50,000 Taiwan Geological Map—Guangfu, 2012). The bedding strike is 062°, 55° dipping to the South, and the attitude changes little. In the field, we indeed observed several high-angle reverse fault systems, as shown in Fig. 3. The fault trends are between 335° and 025° and the dip angle is between 50 and 90 degrees, mainly westward dipping (Fig. 3a).

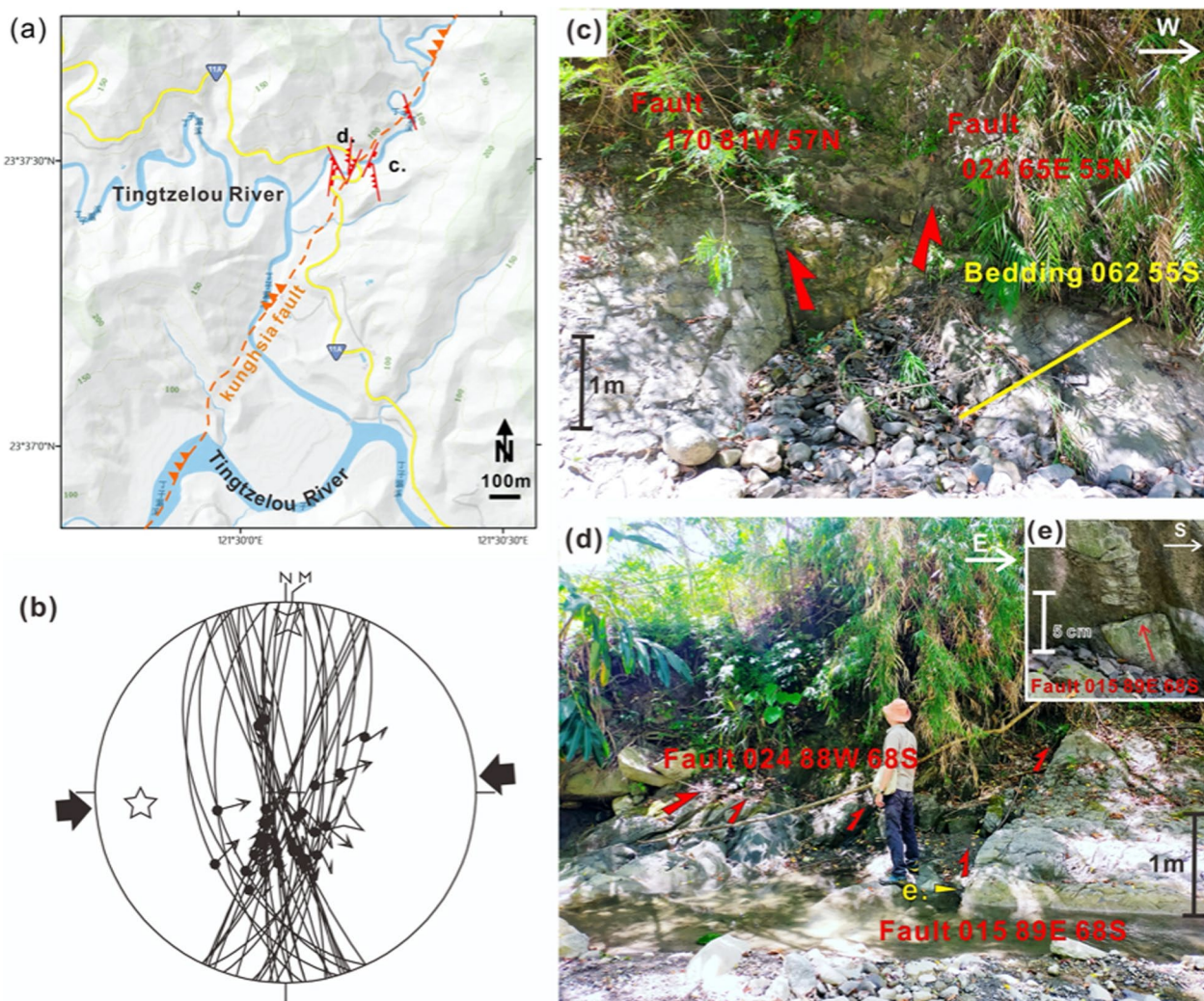


Fig. 3 Field survey results in the Tingtzelou river (location shown in Fig. 1b by blue triangle). **a** The topographic map of the outcrop area. Our observation (the red faults) is very close to the location of the Kunghsia fault (Hsu 1954, 1956). **b** The fault slip data and the reconstructed stress result. The maximum horizontal compression of the area is in the E-W direction. **c** Two high-angle faults were observed in the field; the west-dipping reverse fault (fault 1) is 170, 61W, 57N (strike, dip, pitch), and the east-dipping fault (fault 2) is 024, 65E, 55N, with a normal sense of motion. The orientation of bedding is 062, 55S. **d** A series of high-angle steeply reverse faults of which the strike is from 345 to 015. **e** Re-crystallized slickenside on the eastward turned fault plane. The orientation of slickenside is 015, 89E, 68S but with normal sense movement

However, the high-angle normal faults dipping to the east can also be observed (Fig. 3c). In the steeply reverse fault systems, when the high-angle fault plane turns to east-dipping, the movement transforms to normal sense (Fig. 3d).

Based on the characteristics of re-crystallize slickenside on the fault plane, we get this fault plane is 015° trend and steeply dipping (89°) toward the east, with a normal sense of motion (Fig. 3e). Since these reverse faults and normal faults are all very steep and have very similar orientations, we infer that they belong to the same family and are all related to the high-angle fault mentioned before. We reconstruct the stress by a computer using inverse methods (Angelier 1989, 1990) and represented in stereoplots (Schmidt's projection, lower hemisphere) (Fig. 3b). The result shows the maximum horizontal compression stress is in the E-W direction. The maximum principal stress axis (σ_1) has an inclination of about 30 degrees with the horizontal plane, which means this steep fault has been tilted due to the late tectonic activity. We also calculated the ratio of the principal stress, $\Phi = (\sigma_2 - \sigma_3) / (\sigma_1 - \sigma_3)$ of this area, which the Φ value is 0.923 and represents that the σ_1 and σ_2 of this area are very similar; and the reverse fault can be changed into the strike-slip fault when the trends of σ_1 and σ_2 exchange with each other.

5 Dislocation model simulation

5.1 Tectonic model settings

Based on the integration of geodetic, seismic, and field survey data, we have developed a conjugated structural model. The key parameters of this model are summarized in Table 4. The conjugated structural model spans a total length of 10 km with a strike angle of 30° in the NE-SW direction (Fig. 4a), as determined from the interferograms and LOS results obtained from Sentinel-1A (Fig. 2a and c), alongside focal mechanism analysis. This model comprises two primary fault planes: the main fault plane and the coupled ramp plane (Fig. 4b).

The epicenter of the earthquake occurred on the main fault plane at a depth of 6.8 km. The dipping angle of the main fault plane, set at 30°, aligns with the focal mechanism results. The western boundary of the main fault plane, determined from DInSAR results, lies at the

convergence of the CeR and the LV plain, extending eastward to meet the coupled ramp plane. This fault plane spans a width of 10 km.

The eastern boundary of the coupled ramp plane is inferred from the position of discontinuous interferometric fringes in the DInSAR results, primarily occurring at the junction of the Hsinshe Fault and the Kunghsia Fault. Field investigations have established a dipping angle of 70 degrees for the coupled ramp plane, which connects with the main fault plane to the west. The coupled ramp plane has a width of 4 km.

The depth of the coupled ramp plane ranges from surface level to 3.758 km at its deepest point. This depth is derived from the width of the coupled ramp plane (4 km) multiplied by the sine of 70 degrees. Similarly, the main fault plane ranges in depth from 3.758 km at the bottom of the coupled ramp plane to 8.758 km at its deepest point. This depth is calculated by adding the depth of the coupled ramp plane (3.758 km) to the product of the width of the main fault plane (10 km) multiplied by the sine of 30 degrees.

It's important to note that while the LVF may intersect the boundary of the structural model where both fault planes conjugate, its influence remains constant for the purposes of this earthquake event. Figure 4c illustrates the conceptual model of the conjugated structure.

5.2 Slip displacement estimation

In Sect. 5.1, we adopted a forward approach to delineate the geometric distributions and parameters of the conjugated structural model within our study area. In this section, we utilized the coseismic LOS results from Sentinel-1A to constrain our surface deformation simulation. The goal was to estimate the slip amounts on the main fault plane by minimizing the misfit between the observed LOS data and the simulation results.

While the time period between two Sentinel-1A images may be interpreted as the coseismic period, we must consider that besides coseismic surface deformation induced by the main shock, the discontinuous interferometric fringes indicative of fault structure activity, as well as subsequent aftershocks, could also influence surface displacement. We observed partial aftershocks on the coupled ramp plane, implying that slight displacements occurred on this plane as well. Consequently, during the simulation process, we converted the cumulative energy from the aftershocks within the CoR into slip displacements on the ramp plane, averaging approximately 1 cm.

For the surface deformation simulation, we employed the dislocation model codes developed by Okada (1985), which are well-suited for capturing surface displacements, strains, and tilts resulting from inclined shear and tensile faults in a half-space. To execute this model and

Table 4 The geometric parameters of fault plane for the conjugated structural model

Plane type	Length (km)	Width (km)	Strike (°)	Dip (°)	Slip (cm)
Main fault plane	10	10	30	30	58
Couple ramp plane	10	4	30	70	1

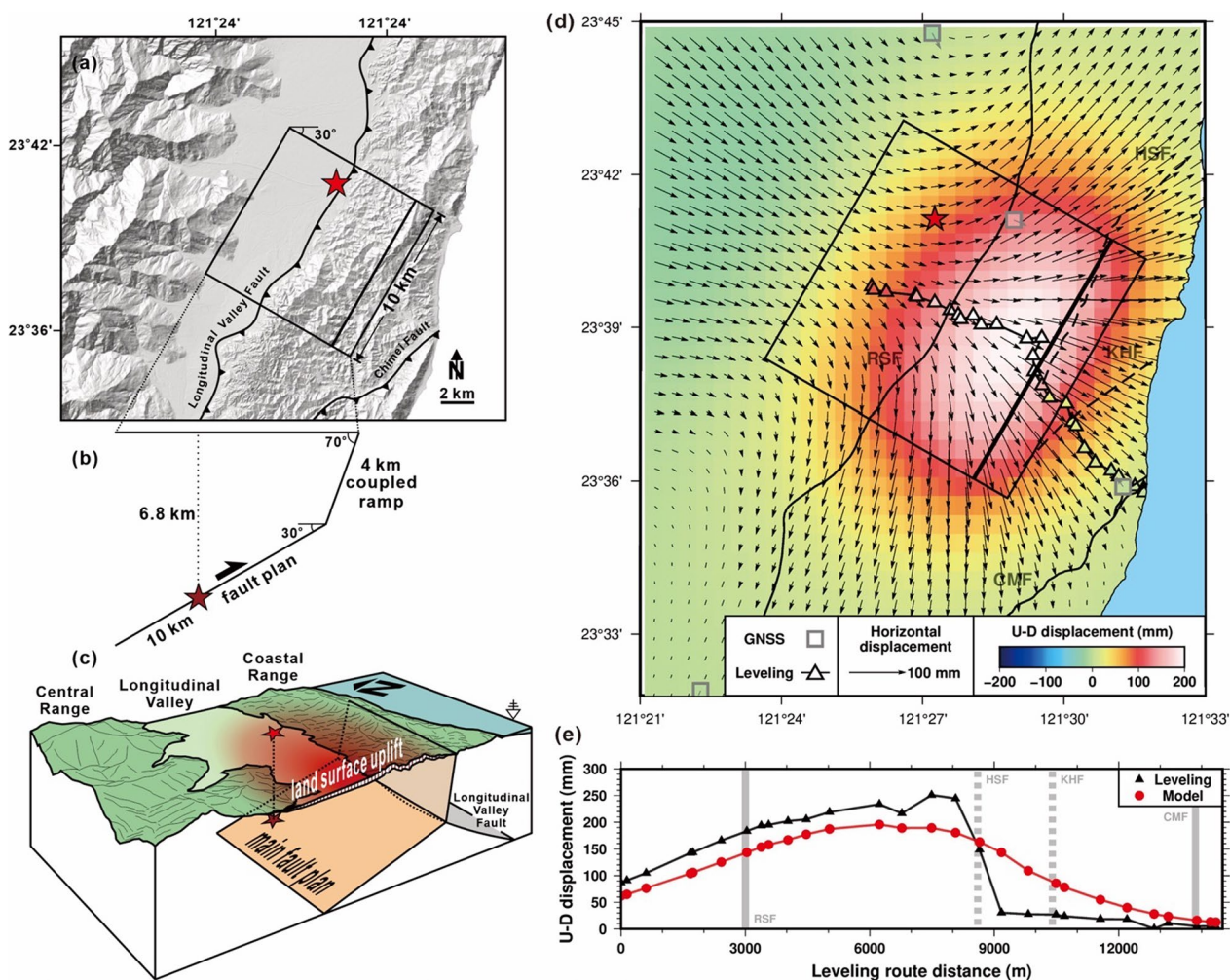


Fig. 4 The conjugated structural model and the simulation results. Viewing the geometric patches of fault planes from **a** above direction and **b** N30° direction. The red star is the hypocenter. **c** The structures model around the study area. **d** The 3D displacements of model simulation. The warmer colors and the arrows indicate the vertical uplift and horizontal displacements, respectively. The gray squares and arrows represent the GNSS 3D data. The black triangles represent the leveling measurement data. **e** The comparison of vertical uplift between simulation results and leveling data

account for the detailed geometric specifications of the faults, we utilized the GTFDef software (Murekezi et al. 2020), which implements the algorithms predominantly derived from Okada’s parameterization of deformation.

By minimizing the misfit between the coseismic LOS results from Sentinel-1A and the dislocation model simulation, we estimated the slip displacement on the main fault plane to be approximately 58 cm. Considering the size of the main plane and the fault slip with a shear modulus of 3×10^{10} N/m², the energy on the main fault plane in the simulation results aligns well with the GSMMA report (2022b).

Their findings, based on continuous GNSS stations, RTK GNSS, and leveling data, suggested a moment magnitude (*M_w*) of 6.17 for the Guangfu earthquake.

Our estimated *M_w*=6.19 closely corresponds to their results and falls within the same order of magnitude as the recorded energy released for the event (*M_w*=5.94), indicating that the model proposed in this study provides a close approximation to the best-fitting fault model solution. However, it’s essential to note that this estimation is based on an idealized slip path on a homogenous material and does not account for energy loss or dispersion, thus, a difference of under one order of magnitude is considered reasonable.

5.3 Surface deformation simulation

Figure 4d displays the 3D surface deformation of simulation results. The colors represent the vertical displacements, with yellow to white indicating uplift and green

to blue indicating subsidence. The length and direction of arrows denote the displacement value and the associated horizontal movement, respectively. In general, the simulation results align with GNSS 3D data in term of both the direction and magnitude of displacements (the colors within the gray squares and the magnitude of gray arrows in Fig. 4d), except for the horizontal movement near the FONB station, which exhibits an opposite horizontal direction. The maximum vertical and horizontal displacements are concentrated on the western side of the CoR with 200 mm uplift and 100 mm horizontal movement.

After the earthquake event, GSMMA (2022b) conducted leveling measurements to understand the vertical displacement of the ground during the earthquake. The leveling measurement data showed that the largest vertical uplift occurred within the CoR on the west side of the HSF with 250 mm, and there was a significant vertical deformation gradient between the HSF and KHF, especially on both sides of the HSF fault (Fig. 4e).

Comparing our simulation results with the leveling measurement data, it is evident that the deformation trends in space are very similar between the two datasets. The greatest discrepancy between the two datasets occurs between the HSF and KHF faults. The source of this discrepancy may arise not only from the different time spans between the Sentinel-1A image pair and the leveling measurement campaign, but also from the potential inaccuracies in the fault parameters set for this region due to other regional fault structures were not considered.

6 Discussion

6.1 The residual between observation and simulation

To assess the difference between observations and simulation, the 3D displacements from coseismic surface deformation in the simulation were projected onto LOS displacements for both the ascending and descending orbits. The LOS results from both satellites cannot be directly compared due to the differences in flight direction, looking angle, and the microwave length. This comparison was conducted for two stages: the first stage corresponds to the coseismic period, while the second stage encompassed both co- and post-seismic periods (Fig. 5). The residuals in the first stage are smaller than in the second stage when comparing the LOS observation from both satellites with the LOS results of the simulation coseismic deformation. This discrepancy suggests the presence of postseismic surface deformation.

In our model, the geological material is assumed to be homogeneous on the fault planes. In reality, the main geological material in the CoR consists of rigid igneous rock with low plasticity, while the LV plain is primarily

composed of fluvial sedimentary rock with fine particles and high compression. In the first stage, the positive residuals observed in the LV plain (the gray rectangle in Fig. 5e) can be attributed to the high-compression geological material being squeezed by the earthquake's force, resulting in deformation with amplification effects. This phenomenon is consistent with the presence of pressure ridge ruptures with an extension direction of N43°E in the riverbed of the LV plain (GSMMA 2022a). In the second stage, the negative residuals observed in the LV plain (the gray rectangle in Fig. 5f) can be linked to a rebound phenomenon in surface deformation during the postseismic period. In addition, the time-series records from the DNFU station show that while the horizontal displacement of the surface continues to increase in the southeast direction after the earthquake, there is a downward trend in the vertical direction starting from September (Fig. 6a). Therefore, the residuals in the LV plain are primarily influenced by the differing material characteristics between the LV plain and the CoR.

Despite the first stage be defined as the coseismic period, the interval between the two Sentinel-1A images also recorded the surface deformation occurring 10 days after the main shock. The location of negative residuals in the CoR (the red circle in Fig. 5e) corresponds to areas where five aftershocks of magnitude greater than 4 and depth less than 10 km occurred. During the simulation procedure, we assumed the slip displacement from the total energy of these aftershocks on the couple ramp plane. However, in reality, the fault slip behavior exhibits anisotropy. In addition, the aftershocks can reduce the coherence of radar image pairs in vegetated areas, leading to phase unwrapping errors.

In the second stage, the negative residuals with ten centimeters in the CoR (the red circle in Fig. 5f) are situated on the boundary between the Paliwan Formation and the Tuluanshan Formation (Wang and Chen 1993) and along the Hsinshe Fault and Kunghsia Fault. The time-series data from the FONB station show that the horizontal surface deformation continues to increase in the northwest direction after the earthquake, while the vertical surface displacement transitions from slight uplift during the coseismic period to slight subsidence in the postseismic period (Fig. 6b). Furthermore, the long-term geodetic observations near the past 15 years indicate the surface deformation moving at a rate of 3 cm/year in the NW direction with 1 cm/year subsidence in this region (Chen et al. 2021). Consequently, the characteristics of the postseismic surface deformation within the CoR may not solely be controlled by the lithologic difference, but may also be influenced by the NW force, driving subsidence along the couple ramp fault, and resulting in the negative LOS residuals for both stages.

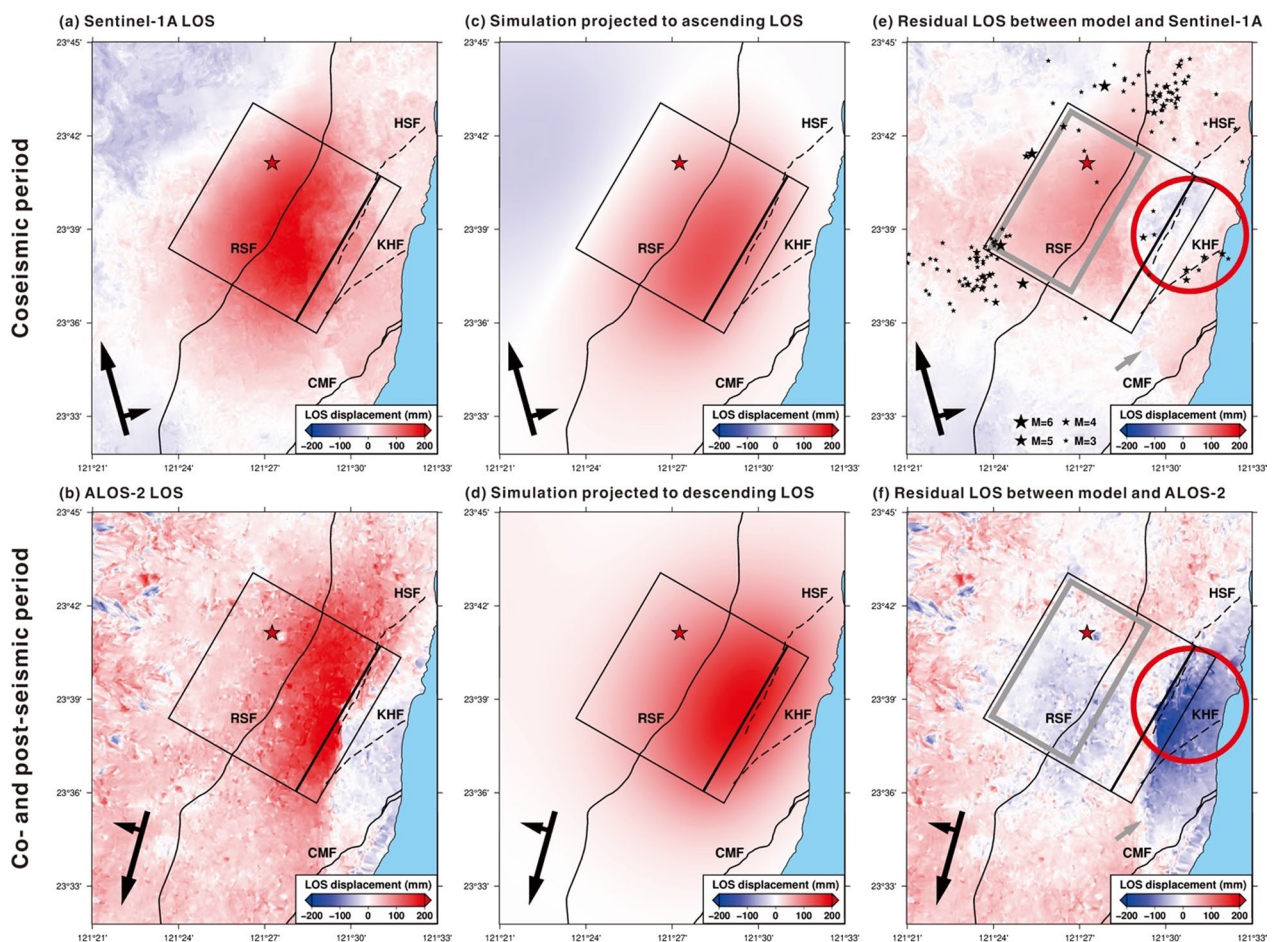


Fig. 5 The InSAR model fitting. The observed InSAR results from **a** Sentinel-1A and **b** ALOS-2. The simulated InSAR results from **c** Sentinel-1A of ascending orbit **d** ALOS-2 of descending orbit. The residuals between simulation and **e** Sentinel-1A and **f** ALOS-2. The RSF is Ruisui Fault; The HSF is Hsinshue Fault; The KHF is Kungshe Fault; The CMF is Chimei Fault. The red star is the hypocenter. The gray rectangles and the red circles indicate the obvious residuals in the LV plain and CoR, respectively. The gray arrows indicated the connection between Chimei Fault and Kunghsia Fault

6.2 The fault features derived from field survey data in the CoR

The Guangfu earthquake's focal mechanism and hypocenter bear a resemblance to the tectonic structure observed during the 2013 Ruisui earthquake (Chuang et al. 2014; Lee et al. 2014). However, if we use geodetic observations to constrain fault parameters based on a similar structural model from the 2013 Ruisui earthquake, there could be uncertainties and mismatches with the actual geological setting. Even with the assistance of geophysical data, such as seismic waves and seismic tomography (Huang et al. 2014), to help the inversion model obtain reliable parameters, the geometry of the fault plane near the surface would still be limited due to the spatial resolution of the data. Therefore, it becomes essential to consider detailed and accurate field survey data. Our field investigations indicated that Kunghsia Fault exists in a steeply reverse fault system. When the

high-angle fault plane turns to east-dipping, the movement transforms to a normal sense. This characteristic is consistent with the significant negative residuals observed on the eastern side of Kunghsia Fault during the second stage (the red circle in Fig. 5f).

Furthermore, although the field survey report (GSMMA 2022a) recorded primary surface cracks along the LVE, the total displacements of these surface cracks do not match the LOS displacement observed from DInSAR results. Additionally, there is no obvious difference in surface displacement on both sides of the LVF (Fig. 2c and d). The maximum surface deformation is concentrated in the western part of the CoR in both stages. Peak ground acceleration data from the P-alert Strong Motion Network (<https://palert.earth.sinica.edu.tw>) recorded values higher than 150 gal distributed in an ellipse shape that matches the area of fringes observed in the DInSAR results (Fig. 2a). Moreover, Huang and Wang (2022)

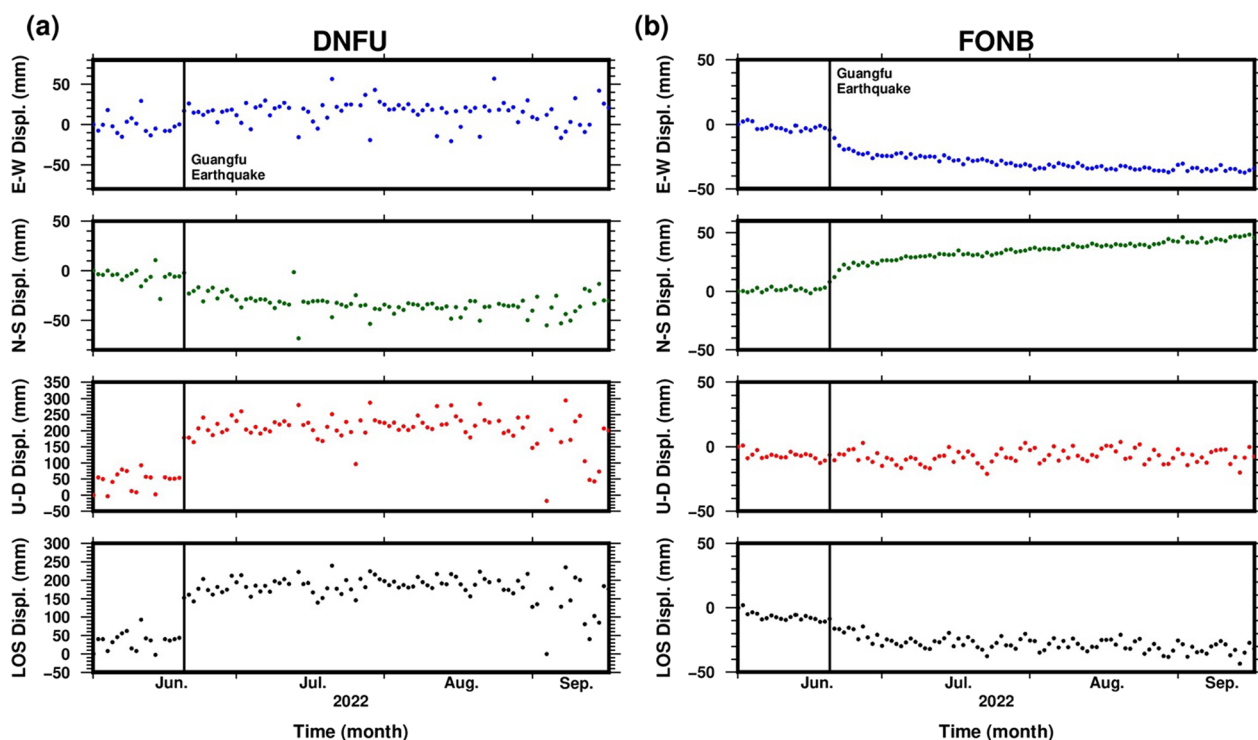


Fig. 6 The time-series displacement from continuous GNSS. **a** DNFU station and **b** FONB station. Both 3D displacements are projected onto the LOS displacements of ALOS-2 satellite for descending orbit

argued that a westward dipping structural boundary exists beneath the CoR, and suggested a tectonic model in which the CeRF cuts across the LVF in the middle segment of the LV. Therefore, it is likely that the surface cracks along the LVF were caused by ground shaking. The primary surface deformation is influenced by the activity of the CeRF, which triggers other older faults within the CoR, even develop the west dipping thrust fault with high angle and reach the ground surface within the CoR, such as the Kunghsia Fault. In this case, the field survey data not only help define the fault features in the CoR but also control the fault geometry near the surface, ultimately improving the reliability of simulation results.

6.3 The significance of Kunghsia Fault between two fault systems

In the northern side of the Tingzelou River, Wang and Chen (1993) described that the Hsinshe Fault as a reverse fault with similar strike and dip angles to the Chimei Fault. Both faults indicated that the Tuluanshan Formation (igneous rocks) thrust on the top of Paliwan Formation (sandstone interbedded with shale) from east to west. On the other hand, the Kunghsia Fault, located between Hsinshe Fault and Chimei Fault, lies on the Paliwan Formation, and its dip direction is opposite to both Hsinshe Fault and Chimei Fault, leading to the

consideration that Hsinshe Fault and Chimei Fault are independent systems.

Nevertheless, based on the interferometric results (Fig. 2a and b) and simulation residuals (the gray arrows indicated in Fig. 5e and f), the distinct linear features in the CoR seem to suggest that Chimei Fault is connected to Hsinshe Fault through Kunghsia Fault. This linear connection is consistent with both the features and the spatial distribution of the Chichi Fault was proposed by Hsu (1956). Therefore, these three old faults within the CoR appear to exhibit interconnected characteristics.

Shyu et al. (2006b) proposed a fault-bend fold model and explained the existence of a high-angle fault plane with eastward dipping in the near-surface geometry of the LVF beneath the CoR. This suggests that there are multiple angular variations in the near-surface structural planes of the LVF. Areas with such angular variations are often more fractured and fragile, making it easier for the CeRF to create a conjugate structure with LVF while moving eastward in a thrusting manner. During this process, CeRF can cut through LVF and continue to develop along old fault planes until reaching the surface, forming as Kunghsia Fault.

Based on such structural conditions, when older faults within the CoR are influenced by the interaction between the active CeRF and LVF, it is plausible that

the original Tuluanshan Formation situated along these older faults may have undergone increased fracturing compared to other areas with the Tuluanshan Formation. This heightened fracturing could render it more susceptible to erosion by the Tingzelou River, eventually leading to its replacement by the Paliwan Formation, which is the result of sedimentation from the Tingzelou River. Both tectonic activity and weathering processes could be contributing factors to why the Kunghsia Fault is positioned on the Paliwan Formation.

In summary, the findings suggest that the Guangfu earthquake was primarily caused by the activity of the CeRF, and the pre-existing fault planes belonging to the LVF system within the CoR exhibited characteristics of reactivation in response to earthquake-triggered processes.

7 Conclusion

This study presents a comprehensive analysis of the 2022 Guangfu earthquake, shedding light on its underlying fault mechanisms and associated surface deformations. The major findings and contributions of this research are as follows:

- (1) The primary active fault responsible for the Guangfu earthquake is identified as the west-dipping CeRF beneath the CeR in the eastern Taiwan.
- (2) During the Guangfu earthquake, the CeRF exhibited approximately 58 cm of eastward reverse slip on its main fault plane. This fault cuts across the LVF beneath the CoR in the middle segment of the LV, and developed a coupled ramp plane along the pre-existing fault planes of the LVF. The combined effect led to approximately 20 cm of vertical surface deformation within the CoR.
- (3) Field investigations were instrumental in providing crucial geometric parameters that facilitated the constraint of near-surface fault planes associated with the coupled ramp plane.
- (4) The observation of a linear connection between the Hsinshe Fault, Kunghsia Fault, and Chimei Fault aligns with the distribution of coupled ramp planes. This suggests that old faults within the CoR exhibit characteristics of reactivation in response to moderate earthquake-triggered processes.
- (5) The study's insights into the conjugate mechanisms of the CeRF and LVF enhance our understanding of subsurface structural activity in the middle segment of the LV. This knowledge holds the potential to improve regional seismic hazard assessment and mitigation efforts in the future.

In summary, this research provides a valuable contribution to the field of seismology and tectonics by unraveling the complexities of fault interactions during the Guangfu earthquake. It underscores the importance of considering both deep and near-surface fault structures when assessing seismic hazard and highlights the significance of detailed geological investigations in advancing our comprehension of earthquake sources and their surface impacts.

Acknowledgements

The authors thank the European Space Agency for supplying the Sentinel-1 SAR images and the GPS Lab, Institute of Earth Science, Academia Sinica, Taiwan, for providing the postseismic GNSS data. Moreover, the authors acknowledge the National Science and Technology Council, Taiwan for the financial supports, MOST 112-2116-M-001-009-MY2, MOST 111-2116-M-008-004-MY3 and 113-2114-M-008-001.

Author contributions

C-HL: Conceptualization, Software, Formal analysis, Visualization, Writing—Original Draft, Funding acquisition, Project administration. Y-CH: Investigation, Formal analysis, Visualization, Writing—Original Draft. C-PC: Conceptualization, Investigation, Visualization, Writing—Review and Editing, Supervision. Y-GC: Conceptualization, Writing—Review and Editing.

Funding

This study was funded by National Science and Technology Council, MOST 112-2116-M-001-009-MY2, Chih-Heng Lu, and MOST 111-2116-M-008-004-MY3 and 113-2114-M-008-001, Chung-Pai Chang.

Data availability

The data supporting the findings of this study are openly available for 4TU. Research Data at <https://doi.org/10.4121/Oe97ae10-87df-4300-a937-f03e10a47353.v1>.

Received: 13 October 2023 Accepted: 14 April 2024

Published online: 13 May 2024

References

- Angelier J (1989) From orientation to magnitudes in paleostress determinations using fault slip data. *J Struct Geol* 11(1–2):37–50. [https://doi.org/10.1016/0191-8141\(89\)90034-5](https://doi.org/10.1016/0191-8141(89)90034-5)
- Angelier J (1990) Inversion of field data in fault tectonics to obtain the regional stress—III. A new rapid direct inversion method by analytical means. *Geophys J Int* 103(2):363–376. <https://doi.org/10.1111/j.1365-246X.1990.tb01777.x>
- Bertiger W, Bar-Sever Y, Dorsey A, Haines B, Harvey N, Hemberger D, Heflin M, Lu W, Miller M, Moore AW, Murphy D, Ries P, Romans L, Sibois A, Sibthorpe A, Szilagyi B, Vallisneri M, Willis P (2020) GipsyX/RTGx, a new tool set for space geodetic operations and research. *Adv Space Res* 66(3):469–489. <https://doi.org/10.1016/j.asr.2020.04.015>
- Biggs J, Wright TJ (2020) How satellite InSAR has grown from opportunistic science to routine monitoring over the last decade. *Nat Commun* 11:3863. <https://doi.org/10.1038/s41467-020-17587-6>
- Chan CH, Ma KF, Shyu JBH, Lee YT, Wang YJ, Gao JC, Yen YT, Rau RJ (2020) Probabilistic seismic hazard assessment for Taiwan: TEM PSHA2020. *Earthq Spectra* 36(S1):137–159. <https://doi.org/10.1177/8755293020951587>
- Chen CW, Zebker HA (2002) Phase unwrapping for large SAR interferograms: statistical segmentation and generalized network models. *IEEE Trans Geosci Remote Sens* 40:1709–1719. <https://doi.org/10.1109/TGRS.2002.802453>
- Chen WS, Yen IC, Fengler KP, Rubin CM, Yang CC, Yang HC, Chang HC, Lin CW, Lin WH, Liu YC, Lin YH (2007) Late Holocene paleoearthquake activity

- in the middle part of the Longitudinal Valley fault, eastern Taiwan. *Earth Planet Sci Lett* 264:420–437. <https://doi.org/10.1016/j.epsl.2007.09.043>
- Chen WS, Wu YM, Yeh PY, Lai YX, Ke MC, Ke SS, Lin YK (2018) Seismogenic structures of the eastern Taiwan collision zone. *Spec Publ Cent Geol Surv* 33:123–155
- Chen HY, Lee JC, Tung H, Chen CL, Lee HK (2021) Variable vertical movements and their deformation behaviors at convergent plate suture: 14-year-long (2004–2018) repeated measurements of precise leveling around middle Longitudinal Valley in eastern Taiwan. *J Asian Earth Sci* 218:104865. <https://doi.org/10.1016/j.jseaeas.2021.104865>
- Cheng WB, Wang C (2001) Seismogenic zones in the convergent margin, eastern Taiwan and its implications in the Luzon forearc deformation. *Terr Atmos Ocean Sci*. [https://doi.org/10.3319/TAO.2001.12.S.269\(ODP\)](https://doi.org/10.3319/TAO.2001.12.S.269(ODP))
- Chuang RY, Johnson KM, Kuo YT, Wu YM, Chang CH, Kuo LC (2014) Active back thrust in the eastern Taiwan suture revealed by the 2013 Ruisuei earthquake: evidence for a doubly vergent orogenic wedge? *Geophys Res Lett* 41:3464–3470. <https://doi.org/10.1002/2014GL060097>
- Chung LH, Chen YG, Wu YM, Shyu JBH, Kuo YT, Lin YN (2008) Seismogenic faults along the major suture of the plate boundary deduced by dislocation modeling of coseismic displacements of the 1951 M7.3 Hualien-Taitung earthquake sequence in eastern Taiwan. *Earth Planet Sci Lett* 269:416–426. <https://doi.org/10.1016/j.epsl.2008.02.035>
- Elliott JR, Walters RJ, Wright TJ (2016) The role of space-based observation in understanding and responding to active tectonics and earthquakes. *Nat Commun* 7:13844. <https://doi.org/10.1038/ncomms13844>
- Geological Survey and Mining Management Agency, MOEA (2022a) 20220620 Guangfu earthquake geological survey report. <https://fault.gsmma.gov.tw/Reports/More/3f0561ae5ffd436b9da65cf8b0a9e0ac>. Accessed 20 Aug 2022
- Geological Survey and Mining Management Agency, MOEA (2022b) 20220620 Guangfu earthquake geological survey report: Geodetic survey for coseismic surface deformation. <https://fault.gsmma.gov.tw/Reports/More/93ec84eb93e24298b4932527525a6fe1>. Accessed 15 Aug 2022
- Hsu TL (1954) Geology Map of the Coastal Range, eastern Taiwan. *Bull Geol Surv Taiwan*
- Hsu TL (1956) Geology of the Coastal Range, eastern Taiwan. *Bull Geol Surv Taiwan* 8:15–41
- Hsu TL (1962) Recent faulting in the Longitudinal Valley of eastern Taiwan. *Memo Geol Soc China* 1:95–102
- Huang HH, Wang Y (2022) Seismogenic structure beneath the northern Longitudinal Valley revealed by the 2018–2021 Hualien earthquake sequences and 3-D velocity model. *Terr Atmos Ocean Sci* 33:17. <https://doi.org/10.1007/s44195-022-00017-z>
- Huang HH, Wu YM, Song XD, Chang CH, Lee SJ, Chang TM, Hsieh HH (2014) Joint Vp and Vs tomography of Taiwan: implications for subduction collision orogeny. *Earth Planet Sci Lett* 392:177–191. <https://doi.org/10.1016/j.epsl.2014.02.026>
- Kuo Chen H, Wu YM, Chang CH, Hu JC, Chen WS (2004) Relocation of eastern Taiwan earthquakes and tectonic implications. *Terr Atmos Ocean Sci* 15(4):647–666. [https://doi.org/10.3319/TAO.2004.15.4.647\(T\)](https://doi.org/10.3319/TAO.2004.15.4.647(T))
- Kuo Chen H, Wu YM, Chen YG, Chen RY (2007) 2003 Mw6.8 Chengkung earthquake and its related seismogenic structures. *J Asian Earth Sci* 31:332–339. <https://doi.org/10.1016/j.jseaeas.2006.07.028>
- Kuo-Chen H, Guan ZK, Sun WF, Zhong PY, Brown D (2019) Aftershock sequence of the 2018 Mw 6.4 Hualien earthquake in eastern Taiwan from a dense seismic array data set. *Seismol Res Lett* 90(1):60–67. <https://doi.org/10.1785/0220180233>
- Lee SJ, Huang HH, Shyu JBH, Yeh TY, Lin TC (2014) Numerical earthquake model of the 31 October 2013 Ruisui, Taiwan, earthquake: Source rupture process and seismic wave propagation. *J Asian Earth Sci* 96:374–385. <https://doi.org/10.1016/j.jseaeas.2014.09.020>
- Lin CW, Liu YC, Chou PS, Lin YH (2021) Recent development of active fault investigations of Taiwan. *Bull Cent Geol Surv* 34:1–40
- Lin CW, Chen WS, Liu YC, Chen PT (2009) Chimei fault. *Spec Publ Cent Geol Surv* 23:55–62
- Murekezi D, Newman A, Feng DL, Chen T (2020) GTDef: georgia tech ground deformation software suite: avnewman/GTDef: GTDef V4 (v4.0.0). Zenodo. <https://doi.org/10.5281/zenodo.4323169>
- Okada Y (1985) Surface deformation due to shear and tensile faults in a half-space. *Bull Seismol Soc Am* 75(4):1135–1154. <https://doi.org/10.1785/BSSA0750041135>
- Rau RJ, Chen KH, Ching KE (2007) Repeating Earthquakes and seismic potential along the northern Longitudinal Valley fault of eastern Taiwan. *Geophys Res Lett* 34:L24301. <https://doi.org/10.1029/2007GL031622>
- Sandwell DT, Mellors R, Tong X, Wei M, Wessel P (2011) GMTSAR: an InSAR processing system based on generic mapping tools. Scripps Institution of Oceanography Technical Report, US San Diego. <https://escholarship.org/content/qt8zq2c02m/qt8zq2c02m.pdf?tid=ilavjh>. Accessed 1 Oct 2023
- Shyu JBH, Sieh K, Chen YG, Liu CS (2005) Neotectonic architecture of Taiwan and its implications for future large earthquakes. *J Geophys Res* 110:B08402. <https://doi.org/10.1029/2004JB003251>
- Shyu JBH, Sieh K, Chen YG, Chung LH (2006a) Geomorphic analysis of the Central Range fault, the second major active structure of the longitudinal Valley Suture, eastern Taiwan. *GSA Bull* 118(11–12):1447–1462. <https://doi.org/10.1130/B25905.1>
- Shyu JBH, Sieh K, Avouac JP, Chen WS, Chen YG (2006b) Millennial slip rate of the longitudinal valley fault from river terraces: implications for convergence across the active suture of eastern Taiwan. *J Geophys Res* 111:B08403. <https://doi.org/10.1029/2005JB003971>
- Shyu JBH, Chung LH, Chen YG, Lee JC, Sieh K (2007) Re-evaluation of the surface ruptures of the November 1951 earthquake series in eastern Taiwan, and its neotectonic implications. *J Asian Earth Sci* 31:317–331. <https://doi.org/10.1016/j.jseaeas.2006.07.018>
- Shyu JBH, Chuang YR, Chen YL, Lee YR, Cheng CT (2016) A new on-land seismogenic structure source database from the Taiwan earthquake Model (TEM) project for seismic hazard analysis of Taiwan. *Terr Atmos Ocean Sci* 27(3):311–323. [https://doi.org/10.3319/TAO.2015.11.27.02\(TEM\)](https://doi.org/10.3319/TAO.2015.11.27.02(TEM))
- Shyu JBH, Yin YH, Chen CH, Chuang YR, Lin SC (2020) Updates to the on-land seismogenic structure source database by the Taiwan Earthquake Model (TEM) project for seismic hazard analysis of Taiwan. *Terr Atmos Ocean Sci* 31(4):469–478. <https://doi.org/10.3319/TAO.2020.06.08.01>
- Wang Y, Chen WS (1993) Geologic map of eastern coastal range scale 1:100,000. Central Geological Survey, MOEA
- Wu YM, Chen YG, Chang CH, Chung LH, Teng TL, Wu FT, Wu CF (2006) Seismogenic structure in a tectonic suture zone: with new constraints from 2006 Mw6.1 Taitung earthquake. *Geophys Res Lett* 33:L22305. <https://doi.org/10.1029/2006GL027572>
- Yen JY, Lu CH, Dorsey RJ, Kuochen H, Chang CP, Wang CC, Chuang RY, Kuo YT, Chiu CY, Chang YH, Bovenga F, Chang WY (2019) Insights into seismogenic deformation during the 2018 Hualien, Taiwan, earthquake sequence from InSAR, GPS, and modeling. *Seismol Res Lett* 90(1):78–87. <https://doi.org/10.1785/0220180228>
- Yi TC, Chen ZY, Lin CW (2012) Geological map of Taiwan scale 1:50,000-Guangfu. Central Geological Survey, MOEA
- Yu SB, Kuo LC (2001) Present-day crustal motion along the longitudinal valley fault, eastern Taiwan. *Tectonophysics* 333:199–217. [https://doi.org/10.1016/S0040-1951\(00\)00275-4](https://doi.org/10.1016/S0040-1951(00)00275-4)
- Yu SB, Chen HY, Kuo LC (1997) Velocity field of GPS stations in the Taiwan area. *Tectonophysics* 274:41–59. [https://doi.org/10.1016/S0040-1951\(96\)00297-1](https://doi.org/10.1016/S0040-1951(96)00297-1)

Publisher's Note

Springer Nature remains neutral with regard to jurisdictional claims in published maps and institutional affiliations.